Analysis of subwavelength bandpass plasmonic filters based on single and coupled slot nanocavities

Xiaoping Zhou[1] and Linjie Zhou[2,*]

[1]Huawei Technologies Co. LTD., Shenzhen 518129, China

[2]State Key Laboratory of Advanced Optical Communication Systems and Networks,
Department of Electronic Engineering, Shanghai Jiao Tong University, Shanghai 200240, China

*Corresponding author: ljzhou@sjtu.edu.cn

Subwavelength surface plasmon polariton optical filters based on metal–insulator–metal slot nanocavites are proposed and analyzed by using coupled mode theory and a finite element method. Simulation results reveal that a single slot cavity coupled with two access waveguides possesses a bandpass-filtering characteristic with its performance affected by its geometric parameters. To further improve the filtering performance, we explore coupled slot cavities as high-order plasmonic filters. When the slot cavities are side-coupled, the bandpass filtering spectrum is dependent on the positions of the access waveguides. The two slot cavities can also be set orthogonal, leading to strong mutual coupling. With careful tuning of the relative length between the two cavities, improved filtering spectrum can be obtained. Given the subwavelength footprint of the proposed plasmonic filters, they can be used in an ultradense plasmonic integrated circuit for optical signal processing.   © 2013 Optical Society of America

OCIS codes: 240.6680, 130.7408, 230.4555, 130.3120.

1. Introduction

The integration density of photonic integrated circuits based on conversional dielectric waveguides is intrinsically limited by the diffraction limit. In order to improve the integration density and make ultradense photonic integrated circuits, plasmonic waveguides based on surface palsmon polaritons (SPPs) are one of the promising solutions [1–4]. The electromagnetic field associated with SPPs is bound at the metal–dielectric interface and decays exponentially toward both sides. The SPPs hence can confine light to a subwavelength scale beyond the diffraction limit. A variety of structures can support plasmon wave propagation, such as metal strips [5], metal V-grooves [6], nanowires [7], nanoparticle chains [8], and metal–insulator–metal (MIM) waveguides [9–11]. Among these various structures, MIM waveguides have attracted considerable research interest as they have the advantages of high optical confinement with reasonable propagation length, zero bending loss, easy fabrication, and flexibility in tuning optical properties. Using MIM plasmonic waveguides, multiple discrete devices have been investigated, including splitters [12], waveguide couplers [13], Mach–Zehnder interferometers [14], Bragg reflectors [15–19], switches [20], etc.

Wavelength-selective bandpass (bandstop) filters, one of the essential elements in optical communication systems, are used to extract (reject) particular wavelength channels from incoming wavelength-division-multiplexing (WDM) data streams. To implement plasmonic filters, interference and resonance structures can be employed. SPP Bragg gratings have been demonstrated to work as broadband filters or reflectors. Introducing a defect in the grating can generate a sharp resonance, which can be used for narrow-band optical filtering. SPP Bragg grating can be implemented by alternatively stacking different dielectric materials in MIM waveguides [16,19], periodically changing the insulator slit width

[15,18,19], or both. Multiple-channel plasmonic filters can be implemented by using Fibonacci-sequence gratings [17]. These grating structures have a relatively large size and a high transmission loss. To make more compact plasmonic filters suitable for nanophotonic integration, ring-, disk-, or rectangle-shaped resonators through various coupling schemes can be employed [21–24]. A simple section of MIM waveguide can be used as a Fabry–Perot (FP) filter when side-coupled with another MIM waveguide [25]. Multiple-channel WDM filters/demultiplexers consisting of a series of nanocapillary resonators with different lengths connected to a common MIM bus waveguide are proposed and studied [26]. The nanocapillary resonators can also be replaced by an array of plasmonic slot cavities to narrow down the filter passband [27]. Recently, MIM waveguides branched with one or multiple stubs have been widely explored as optical filters [28–30]. The resonance effect in the stub structures shows good promise for optical filtering application.

In this paper, narrow-band plasmonic filters based on single or coupled SPP slot resonators are proposed and analyzed. The finite element method (FEM) is used to simulate the filter reflection and transmission spectra along with the resonance mode electromagnetic distribution inside the resonators. We first characterize an optical filter consisting of a single SPP slot cavity. The passband central wavelength and bandwidth can be controlled by selecting proper cavity width and coupling gap size. We then investigate high-order plasmonic filters by using two coupled SPP slot cavities. Two types of arrangements of the cavities with side- and cross-coupling are discussed. The mutual coupling of resonances in the coupled cavities can effectively broaden and flatten the passband while making its roll-off faster.

2. Numerical Method

The MIM waveguide is composed of two metal blocks with a dielectric constant of ε_m and a dielectric layer with a dielectric constant of ε_d sandwiched in between. The light propagation in the MIM waveguide results from the coupled SPP waves along the two metal–dielectric interfaces. The dispersion relation of a MIM waveguide with a width of W can be described by the following equation [31]:

$$\frac{\varepsilon_d p}{\varepsilon_m k} = \frac{1 - e^{kW}}{1 + e^{kW}}. \qquad (1)$$

k and p are defined as

$$k = k_0\sqrt{\beta_{\mathrm{spp}}^2 - \varepsilon_d k_0^2}; \quad p = k_0\sqrt{\beta_{\mathrm{spp}}^2 - \varepsilon_m k_0^2}, \qquad (2)$$

where $\beta_{\mathrm{spp}} = 2\pi n_{\mathrm{eff}}/\lambda$ is the propagation constant of the SPP wave in the MIM waveguide, n_{eff} is the effective refractive index, λ is the free-space wavelength of the incident light, and $k_0 = 2\pi/\lambda$ is the wave number.

In our simulations, we assume the dielectric layer is air and the metal layer is silver (Ag) since silver has low absorption loss in the telecommunication range compared with other metals. Silver can be easily oxidized once exposed to air. For practical fabrication, we can deposit a protection layer to cover the silver surface. The protection layer could be SiO_2, SiN, or other dielectric materials with low absorption loss in the communication wavelength. In this paper, we provide a proof-of-principle numerical study of plasmonic filters with three different structures. In principle, the design method and structures we proposed can be adopted for other, more stable metals like Au, Cu, etc. The frequency-dependent complex relative permittivity of silver is given by the Drude model

$$\varepsilon_m(\omega) = \varepsilon_\infty - \frac{\omega_p}{\omega(\omega + i\gamma)}, \qquad (3)$$

where $\varepsilon_\infty = 3.7$ is the dielectric constant at infinite angular frequency, $\omega_p = 1.38 \times 10^{16}$ Hz is the bulk plasma frequency, ω is the angular frequency of the input light wave, and $\gamma = 2.37 \times 10^{13}$ Hz is the damping frequency of the electron oscillations [15].

We use the FEM to simulate the electromagnetic wave propagation in the plasmonic filter. Because of our computer limitation, only two-dimensional (2D) structures are simulated, but the working principle and design methods are of no difference with real three-dimensional (3D) devices. If the metal layer is thick enough (the third dimension much larger than light wavelength) in real devices, then the 3D SPP waveguide can be approximated by 2D calculation. The FEM solves the partial differential equations by meshing a continuous domain into a set of discrete subdomains. Nonuniform grids are adopted and the grid size is chosen to be 10 times smaller than the dimensions of the corresponding regions in order to get good convergence and accuracy during numerical calculations. The domain of solution is meshed into triangular elements with quadratic Lagrange functions. The calculation window is wider than the cavity so that light waves will not interact with the boundary. We use a perfect magnetic conductor ($H_z = 0$) as the top and bottom boundary constraint. The left and right boundaries are set as input and output ports. We first solve the fundamental transverse magnetic (TM)-polarized (magnetic-field perpendicular to the device plane) SPP waveguide mode and then use it as the excitation source at the input port. The input, transmitted, and reflected powers are recorded as P_{in}, P_{tr}, and P_{rf}, respectively. The time-averaged power can be calculated by integration of the Poynting vector over the input/output plane:

$$P = \left[\int \mathrm{Re}(E \times H^*) \bullet \mathrm{d}S\right]\Big/2. \qquad (4)$$

The transmittance and reflectivity are then expressed as $T = P_{\mathrm{tr}}/P_{\mathrm{in}}$ and $T = P_{\mathrm{rf}}/P_{\mathrm{in}}$,

respectively. The transmission and reflection spectra are obtained by scanning the input wavelength.

3. Theoretical Analysis and Numerical Results

In this part, we present both theoretical analyses and numerical simulations of our proposed plasmonic filters. Three types of filters based on single, side-coupled, and cross-coupled SPP slot cavities are investigated in detail. The dependence of the optical filtering properties on the device structural parameters is analyzed.

A. Single SPP Slot Cavity

Figure 1 shows the schematic of the plasmonic filter consisting of three SPP waveguide sections, with the central one serving as a slot cavity and the other two as input and output access waveguides. The slot cavity has a width of W_c and a length of L_c. The slot cavity is separated from the waveguides by a thin metal wall with a size of g. When incident light traveling along the input SPP waveguide sees the first facet of the slot cavity, part of the light is reflected back into the input SPP waveguide and part of the light is coupled into the cavity due to the thin silver wall. The coupled light can be trapped inside the cavity by the two metal facets to form FP resonances if the round-trip phase is an integer number of 2π (phase-matched). The output SPP waveguide couples the resonance light out of the cavity. Therefore, the SPP slot resonator only selects particular wavelength channels to transmit to the output port.

The SPP slot cavity can be modeled by using the coupled mode theory (CMT) [32]. The amplitudes of the input and reflected light are denoted by s_{+1} and s_{-1}, respectively, and the output light by s_{-2}. They are all normalized to the power in the SPP waveguide. The amplitude of the mode in the cavity is denoted by a, normalized to the energy in the SPP slot cavity. The evolution of the SPP slot cavity mode is described by the CMT equation as

$$\frac{da}{dt} = \left(j\omega_0 - \frac{1}{\tau_0} - \frac{1}{\tau_{e1}} - \frac{1}{\tau_{e2}}\right)a + \kappa_1 s_{+1}, \quad (5)$$

where ω_o is the resonant frequency, $1/\tau_o$ is the decay rate due to SPP slot cavity internal loss, $1/\tau_{e1}$ and $1/\tau_{e2}$ are the rates of external decay into input and output waveguides, respectively, and κ_1 is the input coupling coefficient. The decay rates are related to
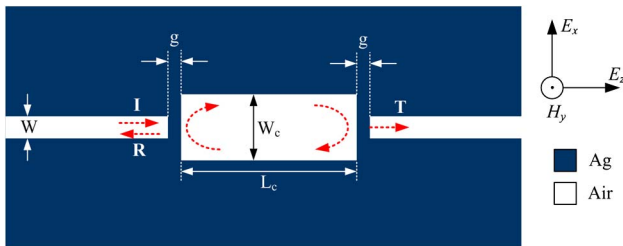

Fig. 1. (Color online) Schematic structure of the plasmonic filter based on a single SPP slot cavity.

the unloaded quality factor and the external quality factors and of the resonator by $Q_o = \omega_o\tau_o/2$, $Q_{e1} = \omega_o\tau_o/2$, $Q_{e2} = \omega_o\tau_o/2$. The reflected and transmitted light waves are given by

$$s_{-1} = -s_{+1} + \kappa_1^* a$$
$$s_{-2} = \kappa_2^* a. \quad (6)$$

The coupling coefficient κ_i ($i = 1, 2$) is related to the delay rate $1/\tau_{ei}$ by power consumption and is given by $\kappa_i = \sqrt{2/\tau_{ei}}e^{j\theta_i}$, where θ_i is the phase change associated with the coupling. Using Eqs. (5) and (6) and assuming input wave $s_{+1} \sim e^{j\omega t}$, we get the filter reflection and transmission functions

$$R = \frac{s_{-1}}{s_{+1}} = \frac{-j(\omega - \omega_o) - \frac{1}{\tau_o} + \frac{1}{\tau_{e1}} - \frac{1}{\tau_{e2}}}{j(\omega - \omega_o) + \frac{1}{\tau_o} + \frac{1}{\tau_{e1}} + \frac{1}{\tau_{e2}}}, \quad (7)$$

$$T = \frac{s_{-2}}{s_{+1}} = \frac{\frac{2}{\sqrt{\tau_{e1}\tau_{e2}}}e^{j(\theta_1 - \theta_2)}}{j(\omega - \omega_o) + \frac{1}{\tau_o} + \frac{1}{\tau_{e1}} + \frac{1}{\tau_{e2}}}. \quad (8)$$

It can be seen that the transmission peak has a Lorenzian lineshape with its bandwidth determined by the total delay rate $1/\tau = 1/\tau_o + 1/\tau_{e1} + 1/\tau_{e2}$. To get higher resonance transmission, the external delay rate $1/\tau_{ei}$ should be higher than the intrinsic delay rate $1/\tau_o$, which implies that the input and output coupling should be strong by using a small gap.

To investigate in more detail the dependence of filtering performance on various design parameters, we perform FEM simulations to study the SPP filter. We first set the cavity width equal to the waveguide width $W_c = W = 50$ nm. The cavity length is $L_c = 0.52$ μm and the total length including the cavity and access waveguides is 1.5 μm. Figures 2(a) and 2(b) show the reflection and transmission spectra for various gap sizes of $g = 10$ nm to 30 nm with a step of 5 nm. The bandpass filtering feature can be clearly observed from the spectra. Figure 2(c) shows the filter central wavelength (resonance wavelength) changes as a function of coupling gap. As the cavity length is only 0.52 μm, the resonance mode is corresponding to the fundamental (first-order) longitudinal mode of the slot cavity. It can be seen that the resonance wavelength experiences a blue-shift from 1610 to 1539 nm with the increase of coupling gap, which suggests a smaller gap gives more phase shift upon reflection on the metal wall. Figure 2(d) shows the insertion loss and bandwidth variation with the coupling gap. The insertion loss is defined as the transmittance at the resonance wavelength, which measures the light transmission efficiency through the SPP slot cavity. The bandwidth is defined as the 3 dB width of the resonance peak in the transmission spectrum. At $g = 10$ nm, the insertion loss is only 2.54 dB while the bandwidth is relatively large (65 nm), corresponding to a resonance quality factor (Q-factor) of 25. When the gap increases to
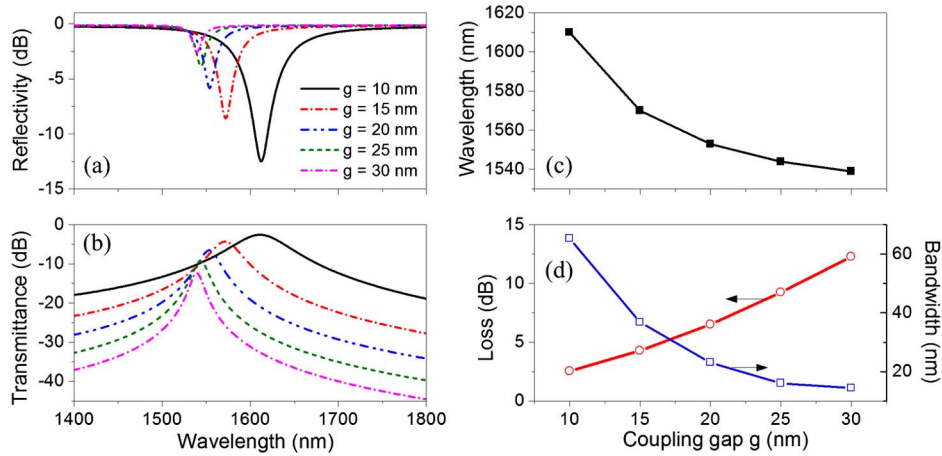
Fig. 2. (Color online) (a) Reflection and (b) transmission spectra of the plasmonic filter based on a single SPP slot cavity for various coupling gap sizes. (c) Filter central wavelength versus coupling gap. (d) Filter insertion loss and bandwidth versus coupling gap.

$g = 30$ nm, the insertion loss increases to 12.3 dB while the transmission peak narrows down to 14 nm, corresponding to an improved Q-factor of 110. The reduced transmittance and narrowed bandwidth are owing to the weakened coupling when the metal wall becomes thicker (larger g). As the metal skin depth is very small (approximately 20 nm at 1550 nm), the metal wall thickness needs to be comparable in order to allow efficient light to couple into the cavity. A small variation in coupling gap will change the coupling significantly, which imposes a challenge for device fabrication.

The filtering performance is dependent on the slot cavity loss including the reflection loss at the metal walls and the light propagation loss in the cavity waveguide. One effective way to reduce the SPP propagation loss is to widen the dielectric slot so that more optical power is located in the slot. We fix the coupling gap at $g = 20$ nm and vary the cavity width W_c to study its filtering performance. The other parameters are the same with the previous case.

Figures 3(a) and 3(b) show the reflection and transmission spectra with the cavity width W_c changing

from 70 to 190 nm with a step of 20 nm. Figure 3(c) shows the filter central wavelength shift with the cavity width. Widening the cavity gradually blueshifts the central wavelength, since the effective refractive index of the MIM SPP waveguide reduces with the increasing slot width. Figure 3(d) shows the insertion loss and the bandwidth change with the cavity width. When the cavity becomes wider, the insertion loss first decreases and then slightly increases after reaching the minimum value of 4.4 dB at $W_c = 150$ nm. There are two factors that affect the insertion loss: the coupling efficiency through the metal wall and the propagation loss of the cavity waveguide, both of which decrease with the cavity width. The coupling efficiency decreases because of the larger mode mismatch between the access and the cavity waveguides. When the cavity width is small (>150 nm), the propagation loss decreases faster than the coupling efficiency, and therefore, the transmission sees a net increase in optical power at the resonance wavelength. The situation is inversed when the cavity becomes too wide (>150 nm). The filtering bandwidth monotonically
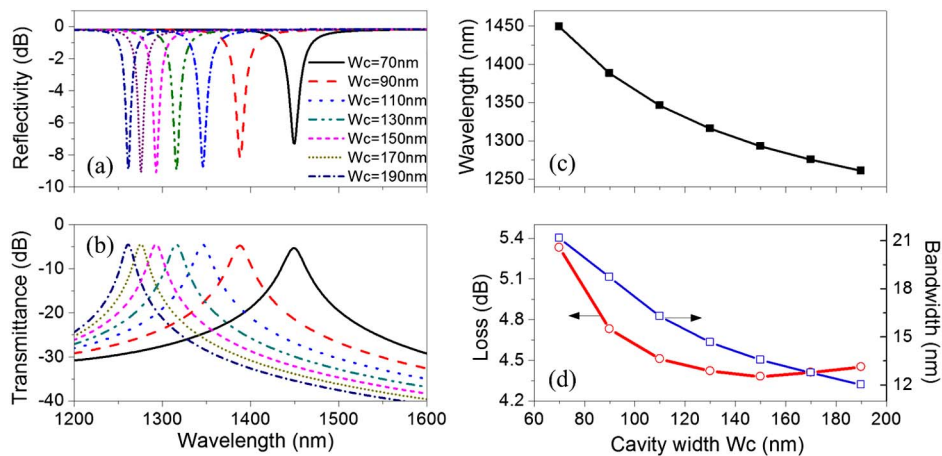

Fig. 3. (Color online) (a) Reflection and (b) transmission spectra of the plasmonic filter based on a single SPP slot cavity for various cavity widths. (c) Filter central wavelength versus coupling gap. (d) Filter insertion loss and bandwidth versus coupling gap.

decreases with the cavity width since the light round-trip loss is reduced. At $g = 150$ nm, the bandwidth is 13.5 nm, corresponding to a Q-factor of 96.

B. Side-Coupled SPP Slot Cavities

The SPP slot cavities can be side-coupled to get a second-order filtering feature. Figures 4(a) and 4(b) show the two configurations of plasmonic filters based on side-coupled SPP slot cavities. The first configuration (type I) has the two access waveguides connected to one common cavity, and the second (type II) to individual cavities. The two SPP slot cavities are separated by a gap of g_c. They have the same width W_c, but their lengths L_{c1} and L_{c2} are not necessarily equal.

With the CMT, the time rate equations of the two coupled SPP slot cavities configured with type I are given by

$$\frac{da_1}{dt} = \left(j\omega_1 - \frac{1}{\tau_{10}} - \frac{1}{\tau_{e1}} - \frac{1}{\tau_{e2}}\right)a_1 + \kappa_1 s_{+1} - j\mu a_2$$
$$\frac{da_2}{dt} = \left(j\omega_2 - \frac{1}{\tau_{20}}\right)a_2 - j\mu a_1, \quad (9)$$

where ω_1 and ω_2 are the resonant frequencies of the two cavities and μ is their mutual coupling coefficient. The reflection and transmission CMT equations are similar to Eq. (6) with only a replaced by a_1. Thus, the filter reflection and transmission functions are derived as

$$R = \frac{s_{-1}}{s_{+1}}$$
$$= -\frac{\left[j(\omega - \omega_1) + \frac{1}{\tau_{10}} - \frac{1}{\tau_{e1}} + \frac{1}{\tau_{e2}}\right]\left[j(\omega - \omega_2) + \frac{1}{\tau_{20}}\right] + \mu^2}{\left[j(\omega - \omega_1) + \frac{1}{\tau_{10}} + \frac{1}{\tau_{e1}} + \frac{1}{\tau_{e2}}\right]\left[j(\omega - \omega_2) + \frac{1}{\tau_{20}}\right] + \mu^2}, \quad (10)$$

$$T = \frac{s_{-2}}{s_{+1}}$$
$$= \frac{\frac{2}{\sqrt{\tau_{e1}\tau_{e2}}}e^{j(\theta_1 - \theta_2)}\left[j(\omega - \omega_2) + \frac{1}{\tau_{20}}\right]}{\left[j(\omega - \omega_1) + \frac{1}{\tau_{10}} + \frac{1}{\tau_{e1}} + \frac{1}{\tau_{e2}}\right]\left[j(\omega - \omega_2) + \frac{1}{\tau_{20}}\right] + \mu^2}. \quad (11)$$

It can be seen that the filter is a second-order filter with the mutual coupling affecting the separation of the poles and thus the filter bandwidth. For the type II configuration, the CMT equations for the coupled cavities are

$$\frac{da_1}{dt} = \left(j\omega_1 - \frac{1}{\tau_{10}} - \frac{1}{\tau_{e1}}\right)a_1 + \kappa_1 s_{+1} - j\mu a_2$$
$$\frac{da_2}{dt} = \left(j\omega_2 - \frac{1}{\tau_{20}} - \frac{1}{\tau_{e2}}\right)a_2 - j\mu a_1. \quad (12)$$

The reflected and transmitted light waves are described by Eq. (6) with a replaced by a_1 and a_2 in the reflection and transmission equations, respectively. R and T are then expressed as

$$R = \frac{s_{-1}}{s_{+1}}$$
$$= -\frac{\left[j(\omega - \omega_1) + \frac{1}{\tau_{10}} - \frac{1}{\tau_{e1}}\right]\left[j(\omega - \omega_2) + \frac{1}{\tau_{20}} + \frac{1}{\tau_{e2}}\right] + \mu^2}{\left[j(\omega - \omega_1) + \frac{1}{\tau_{10}} + \frac{1}{\tau_{e1}}\right]\left[j(\omega - \omega_2) + \frac{1}{\tau_{20}} + \frac{1}{\tau_{e2}}\right] + \mu^2}, \quad (13)$$

$$T = \frac{s_{-2}}{s_{+1}}$$
$$= \frac{\frac{2\mu}{\sqrt{\tau_{e1}\tau_{e2}}}e^{j(\theta_1 - \theta_2 - \pi/2)}}{\left[j(\omega - \omega_1) + \frac{1}{\tau_{10}} + \frac{1}{\tau_{e1}}\right]\left[j(\omega - \omega_2) + \frac{1}{\tau_{20}} + \frac{1}{\tau_{e2}}\right] + \mu^2}. \quad (14)$$

These are the frequency responses of a second-order filter, similar to the type I configuration. The only difference is that the transmission function of type II has only two poles, but there is an extra zero in type I.

To numerically analyze the side-coupled SPP filter performance, we set the intercavity gap $g_c = 70$ nm, the first cavity length $L_{c1} = 520$ nm, and the second cavity length L_{c2} varied. The length difference between the two cavities is defined as $dL_c = L_{c2} - L_{c1}$ The other parameters are the same with the previous case. Figures 5(a)–5(c) show the reflection and transmission spectra for the configuration sketched in Fig. 4(a). It can be seen that two resonance peaks appear in the spectra corresponding to the two poles
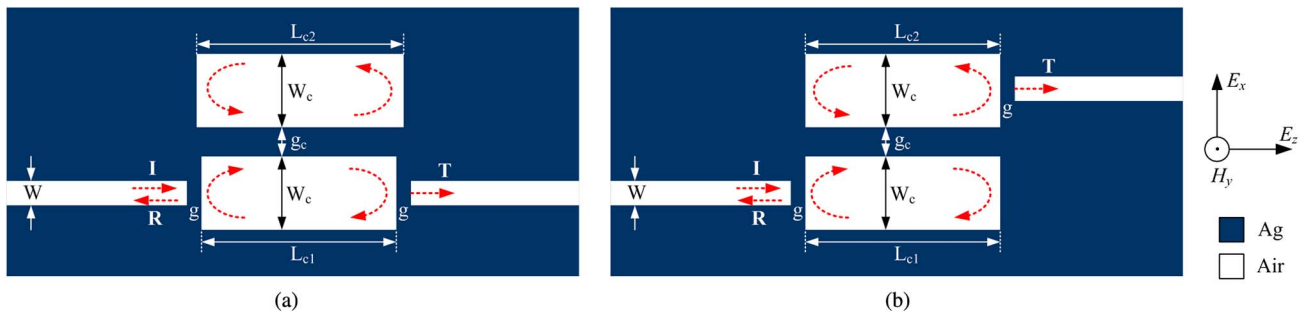

Fig. 4. (Color online) Schematic structures of plasmonic filters based on two side-coupled SPP slot cavities. The output waveguide can either be directly coupled with (a) the first cavity (type I) or (b) the second cavity (type II).

in Eq. (11). When the two cavities are identical ($dL_c = 0$), the right main peak is only slightly shifted away by 5 nm from the original resonance wavelength (indicated by the dot-dashed curve), while the left small peak is 18 nm away. The asymmetry is caused by the unequal resonances from the two cavities. Inspecting Fig. 2, we see that the access waveguides have a significant impact on the resonance of the slot cavity, especially the resonance wavelength. Therefore, the first cavity, end-coupled with the two access waveguides, has a longer resonance wavelength than the second one. In order to compensate for the resonance mismatch, we can slightly increase the second cavity length. The results are presented in Figs. 5(b) and 5(c). Only when the two cavities are optically identical ($dL_c = 5$ nm) with coincident resonances do the spectra show symmetric resonance line shapes. The two resonance peaks are still present when the cavities are balanced due to the coupling induced resonance splitting. The splitting level is dependent on the intercavity mutual coupling strength. Figures 5(d)–5(f) show the spectra when $dL_c = 5$ nm and g_c is increased from 80 to 100 nm. At $g_c = 100$ nm, the transmission spectrum shows a flat top with an insertion loss of 5.3 dB. The filter bandwidth is broadened to 16.76 nm. The electromagnetic fields (H_y and E_x components) at the filter central wavelength are shown in Figs. 5(g) and 5(h). The magnetic fields are out-of-phase in the two cavities. Figure 5(i) shows the time-averaged optical power flow (only magnitude) in the structure. It reveals that power only flows through the first cavity without flowing through the second one (apart from dissipation). The second cavity works like a reservoir to store optical energy therein.

From the above analysis, it can be seen that the length of second cavity should be precisely controlled in order to produce a second-order filter. Alternatively, we can move the output waveguide to the second cav-

ity to make the two cavities symmetrical, as depicted in Fig. 4(b). In this case, the cavity lengths are set to be equal ($L_{c2} = L_{c1}$). Figures 6(a) and 6(b) show the reflection and transmission spectra with various coupling gap sizes. As expected, the two cavities are equally excited, resulting in a symmetrical resonance line shape. At $g_c = 70$ nm, the passband possesses a flat-top with an insertion loss of 6.9 dB and a bandwidth of 15.2 nm. Figures 6(c)–6(e) show the electromagnetic field components and time-averaged optical power flow distributions at the filter central wavelength with $g_c = 70$ nm. Optical power flows through both cavities before reaching the output waveguide as opposed to the previous case.

C. Cross-Coupled SPP Slot Cavities

The last filter structure that we study is composed of cross-coupled SPP slot cavities, as shown in Fig. 7. In this case, the second SPP slot cavity is put vertically across the first one. To simplify our analysis, we assume they are aligned at the cavity center.

We can use the same set of CMT Eqs. (9) and (10) as for the side-coupled SPP filter (type I) to describe the mode evolution. In the cross-coupled SPP cavities, coupling is enabled by the crossing, which is much stronger than the evanescent coupling through the metal wall. The resonance generation in the vertical cavity (or the stub) has been discussed in the literature [18,29,30]. When light encounters the crossing, partial light propagates through and partial light is coupled into the two stubs of the vertical cavity. The reflected light from the two stubs could then interfere with the transmitted light to form resonance at specific wavelengths. A strong mutual coupling means a large μ in the CMT equations. The resonant frequencies of the two cavities can be separately controlled by their cavity sizes, providing a means to tailor the transmission passband by setting proper pole positions.
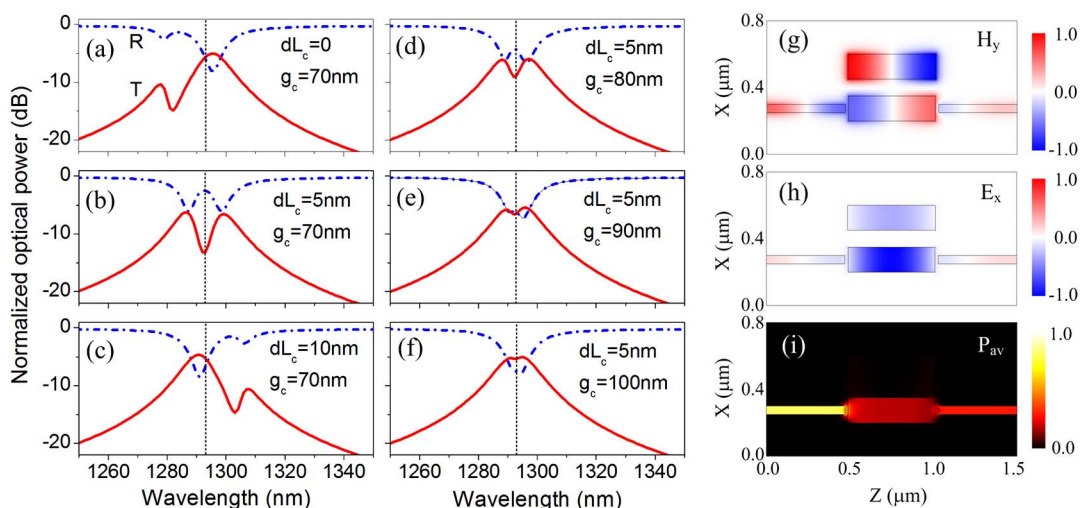

Fig. 5. (Color online) (a)–(c) Reflection and transmission spectra of the plasmonic filter based on side-coupled SPP slot cavities (type I) for various cavity length differences. The intercavity gap is $g_c = 70$ nm. (d)–(f) Reflection and transmission spectra for various intercavity gap sizes. The cavity length difference is $dL_c = 5$ nm. (g) Magnetic field H_y, (h) electric field E_x, and (i) time-averaged power flow magnitude P_{av} distributions at the filter central wavelength with $dL_c = 5$ nm and $g_c = 100$ nm.
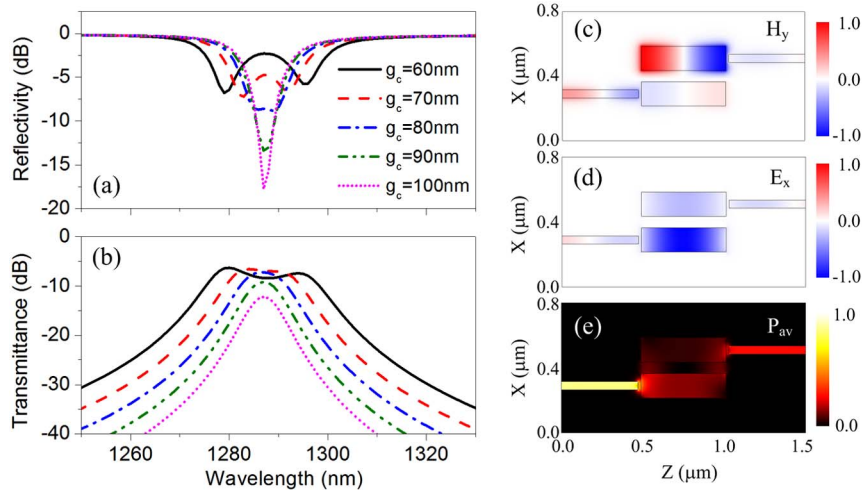
Fig. 6. (Color online) (a) Reflection and (b) transmission spectra of plasmonic filter based on side-coupled SPP slot cavities (type II) for various intercavity gap sizes. (c) Magnetic-field H_y, (d) electric-field E_x, and (e) time-averaged power flow magnitude P_{av} distributions at the filter central wavelength with $g_c = 70$ nm.

We fix the lateral cavity length at $L_{c1} = 520$ nm and vary the vertical cavity length L_{c2} to study its filtering performance with FEM simulations. The solid curves in Figs. 8(a) and 8(b) show the reflection and transmission spectra of a single vertical cavity (without the lateral one). Total reflection occurs at 894 nm. With a lateral cavity of equal length incorporated, the resonances become richer due to the coupling between these two cavities. There are three wavelengths (labeled as A, B, and C) worthy of attention. Comparing the two transmission spectra in Fig. 8(b), we find the deep notch A comes from the vertical cavity only. Figure 8(c) shows the magnetic-field H_y distribution, confirming light is indeed reflected by the crossing. To better understand the origin of the resonance peaks B and C, we also plot their magnetic-field distributions in Figs. 8(d) and 8(e), respectively. It reveals that resonance B results from both cavities and resonance C is from the lateral cavity only. The simulation result is consistent with our theoretical analysis. The notch and peaks correspond to the zero and poles in the transmission Eq. (11), respectively.

From the above analysis, we can see resonance B can be shifted by altering the vertical cavity length. Hence, it is possible to get a high-order passband if resonance B is merged with resonance C. Figures 9(a)

and 9(b) show the spectra when they are close enough with appropriate cavity lengths, together with the original one ($dL_c = 0$). Because of the mutual coupling between the lateral and vertical cavities, the filter bandwidth is increased from 14 to 18 nm with a relatively flat top ($dL_c = 124$ and 148 nm). It should be noted that notch A also moves closer, making the transmittance drop faster at one side (the other side also a little bit faster than the original one). The fast roll-off helps to reduce the cross-talk between adjacent channels. Figures 9(c)–9(e) show the electromagnetic fields and time-averaged power flow distributions at the filter central wavelength for $dL_c = 124$ nm, and Figs. 9(f)–9(h) show the distributions for $dL_c = 148$ nm. From the wave front of H_y distribution, it can be seen light travels and resonates between one lateral stub and the other three in the cross-coupled cavities. In the special case when resonance A is coincident with resonance C ($dL_c = 136$ nm), the transmission peak is split into two due to the strong mutual coupling. The transmittance is reduced to < -13 dB while the reflectivity still remains low (-12 dB) at the filter central wavelength. Most of the incoming optical power is dissipated in the cross-coupled cavities in this case.

4. Discussion

There are multiple ways to implement plasmonic filters, as discussed in the introduction. Our filter is superior to those formed by Bragg gratings in terms of footprint and transmission loss. For example, in Han's plasmonic filter [15], the achievable Q-factor is 80 with 728 nm defect length and eight 660 nm-long Bragg cells on both sides. Therefore, the filter length is longer than 10 um with high transmission loss. To get a higher Q-factor, even more Bragg cells are needed, further increasing the length. The long length of Bragg grating is expected since the reflection of one Bragg cell is low and multiple Bragg cells are necessary to enhance the reflection.
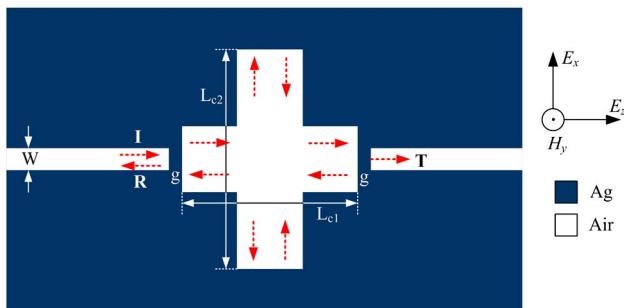

Fig. 7. (Color online) Schematic structure of the plasmonic filter based on two cross-coupled SPP slot cavities.
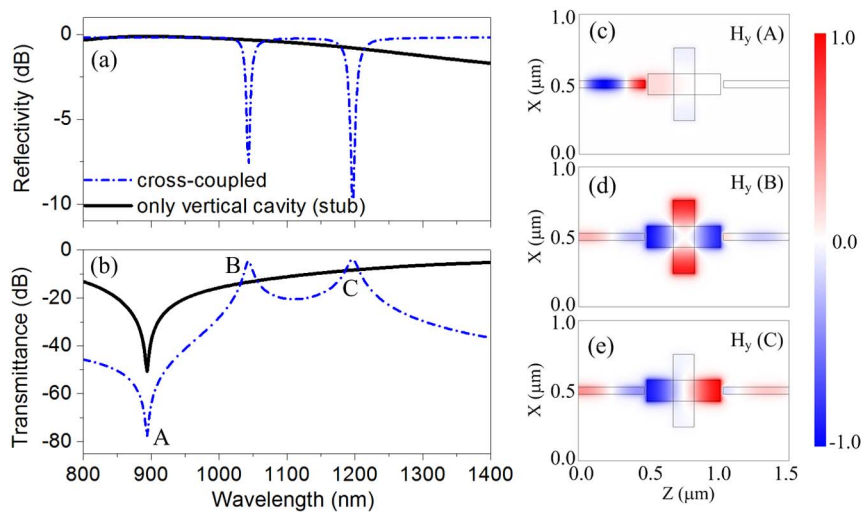
Fig. 8. (Color online) (a) Reflection and (b) transmission spectra of the plasmonic filter based on cross-coupled SPP slot cavities ($L_{c1} = L_{c2}$) and a single vertical cavity. (c)–(e) Magnetic-field H_y distributions in the filter corresponding to three wavelengths of interest: (c) notch A, (d) peak B, and (e) peak C. Their spectral positions are indicated in (b).

Another type of plasmonic filters is based on ring-, disk-, or rectangle-shaped resonators [21–23]. Our single slot nanocavity performance is similar to these structures, as essentially the resonances are all formed by back reflection on cavity metal sidewalls. However, in the existing literature, only plasmonic filters made up of one single nanocavity are investigated, where the resonance spectral profile is a Lorentzian lineshape with a relatively slow roll-off. For practical filtering applications, however, the passband should be flat and the roll-off should be fast to suppress interchannel crosstalk. Therefore, a single cavity based plasmonic filter is not enough. To this end, we proposed cascaded plasmonic nanocavities as higher-order bandpass filters. As discussed in the previous section, the filter spectral profiles of the side-coupled and cross-coupled slot cavities are closer to an ideal box-like shape. The circular-shape nano-

cavities could also be cascaded, but the intercavity coupling is much more difficult to control than the slot SPP nanocavities due to the curved cavity sidewall.

Our proposed SPP filters have the key merit of small footprint in the order of hundreds of nanometers, several orders smaller than conventional approaches based on dielectric waveguides. This feature makes them very attractive for optical signal processing in ultradense nanoscale plasmonic integrated circuits. The nanoscale SPP filters are really comparative in size with today's high-end transistors (tens of nanometers size). Therefore, they hold the potential for hybrid integration with nanoelectronics. They can also work as a bridge to link photonic and microelectronic worlds. Like other plasmonic devices, loss is always inevitable due to the metal ohmic loss. Actually, there is a trade-off between loss and size of plasmonic devices, as high confinement means
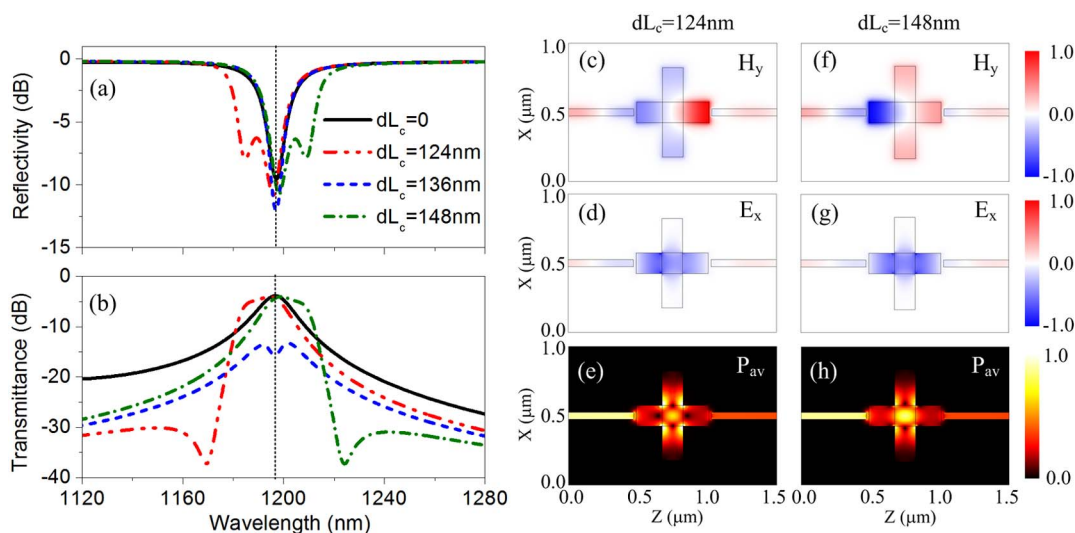

Fig. 9. (Color online) (a) Reflection and (b) transmission spectra of the plasmonic filter based on cross-coupled SPP slot cavities. The vertical cavity length is varied. (c) Magnetic-field H_y, (d) electric-field E_x, and (e) time-averaged power flow magnitude P_{av} distributions at the filter central wavelength indicated by the dotted curves in (a) and (b) for $dL_c = 124$ nm. (f)–(h) are the distribution for $dL_c = 148$ nm.

more interaction of light with metal, thereby leading to a higher absorption loss. In our devices, apart from the metal absorption loss, the return loss due to incomplete resonant tunneling is another source for the low passband transmission (5–10 dB loss). This return loss can be further reduced by enhancing the waveguide-resonator coupling, i.e., decreasing the gap size to 10 nm or even less. However, it should be noted such a small gap makes a great challenge for device fabrication.

5. Conclusions

In summary, subwavelength plasmonic filters based on SPP slot cavities were modeled using the CMT and numerically studied using FEM simulations. Three types of resonant structures composed of single, side-coupled, and cross-coupled SPP slot cavities were investigated. The single slot plasmonic filter has a Lorenzian lineshape passband with its central wavelength, bandwidth, and insertion loss dependent on the cavity size and coupling gap. The side-coupled slot cavities broaden and flatten the passband resulting in a second-order filter. In particular, we considered two configurations to position the output waveguide, either connecting to the first cavity or the second one. It revealed that the latter arrangement can ease the design because the two cavities are equally balanced. We also explored cross-coupled slot cavities as an optical filter. With properly designed cavity dimensions, the resonators can be mutually coupled to also work as a second-order filter. Owing to their very compact sizes in the order of hundreds of nanometers, the plasmonic filters can be used as a basic building block for future nanophotonic integrated circuits.

References

1. S. Lal, S. Link, and N. J. Halas, "Nano-optics from sensing to waveguiding," Nat. Photonics **1**, 641–648 (2007).
2. S. A. Maier, P. G. Kik, H. A. Atwater, S. Meltzer, E. Harel, B. E. Koel, and A. A. G. Requicha, "Local detection of electromagnetic energy transport below the diffraction limit in metal nanoparticle plasmon waveguides," Nat. Mater. **2**, 229–232 (2003).
3. E. Ozbay, "Plasmonics: merging photonics and electronics at nanoscale dimensions," Science **311**, 189–193 (2006).
4. D. K. Gramotnev and S. I. Bozhevolnyi, "Plasmonics beyond the diffraction limit," Nat. Photonics **4**, 83–91 (2010).
5. P. Berini, "Plasmon-polariton waves guided by thin lossy metal films of finite width: bound modes of symmetric structures," Phys. Rev. B **61**, 10484 (2000).
6. D. F. P. Pile and D. K. Gramotnev, "Plasmonic subwavelength waveguides: next to zero losses at sharp bends," Opt. Lett. **30**, 1186–1188 (2005).
7. A. L. Pyayt, B. Wiley, Y. Xia, A. Chen, and L. Dalton, "Integration of photonic and silver nanowire plasmonic waveguides," Nat. Nanotechnol. **3**, 660–665 (2008).
8. S. A. Maier, P. G. Kik, and H. A. Atwater, "Observation of coupled plasmon-polariton modes in Au nanoparticle chain waveguides of different lengths: estimation of waveguide loss," Appl. Phys. Lett. **81**, 1714 (2002).
9. J. Dionne, H. Lezec, and H. A. Atwater, "Highly confined photon transport in subwavelength metallic slot waveguides," Nano Lett. **6**, 1928–1932 (2006).
10. J. Dionne, L. Sweatlock, H. Atwater, and A. Polman, "Plasmon slot waveguides: towards chip-scale propagation with subwavelength-scale localization," Phys. Rev. B **73**, 035407 (2006).
11. P. Neutens, P. Van Dorpe, I. De Vlaminck, L. Lagae, and G. Borghs, "Electrical detection of confined gap plasmons in metal–insulator–metal waveguides," Nat. Photonics **3**, 283–286 (2009).
12. G. Veronis and S. Fan, "Bends and splitters in metal-dielectric-metal subwavelength plasmonic waveguides," Appl. Phys. Lett. **87**, 131102 (2005).
13. R. A. Wahsheh, Z. Lu, and M. A. G. Abushagur, "Nanoplasmonic couplers and splitters," Opt. Express **17**, 19033–19040 (2009).
14. B. Wang and G. P. Wang, "Surface plasmon polariton propagation in nanoscale metal gap waveguides," Opt. Lett. **29**, 1992–1994 (2004).
15. Z. Han, E. Forsberg, and S. He, "Surface plasmon Bragg gratings formed in metal–insulator–metal waveguides," IEEE Photon. Technol. Lett. **19**, 91–93 (2007).
16. J. Park, H. Kim, and B. Lee, "High order plasmonic Bragg reflection in the metal–insulator–metal waveguide Bragg grating," Opt. Express **16**, 413–425 (2008).
17. Y. Gong, X. Liu, and L. Wang, "High-channel-count plasmonic filter with the metal–insulator–metal Fibonacci-sequence gratings," Opt. Lett. **35**, 285–287 (2010).
18. Y. Liu and J. Kim, "Characteristics of plasmonic Bragg reflectors with insulator width modulated in sawtooth profiles," Opt. Express **18**, 11589–11598 (2010).
19. A. Hosseini and Y. Massoud, "A low-loss metal–insulator–metal plasmonic Bragg reflector," Opt. Express **14**, 11318–11323 (2006).
20. C. Min and G. Veronis, "Absorption switches in metal-dielectric-metal plasmonic waveguides," Opt. Express **17**, 10757–10766 (2009).
21. H. Lu, X. Liu, D. Mao, L. Wang, and Y. Gong, "Tunable bandpass plasmonic waveguide filters with nanodisk resonators," Opt. Express **18**, 17922–17927 (2010).
22. T. B. Wang, X. W. Wen, C. P. Yin, and H. Z. Wang, "The transmission characteristics of surface plasmon polaritons in ring resonator," Opt. Express **17**, 24096–24101 (2009).
23. I. Zand, A. Mahigir, T. Pakizeh, and M. S. Abrishamian, "Selective-mode optical nanofilters based on plasmonic complementary split-ring resonators," Opt. Express **20**, 7516–7525 (2012).
24. A. Hosseini and Y. Massoud, "Nanoscale surface plasmon based resonator using rectangular geometry," Appl. Phys. Lett. **90**, 181102 (2007).
25. Q. Zhang, X. G. Huang, X. S. Lin, J. Tao, and X. P. Jin, "A subwavelength coupler-type MIM optical filter," Opt. Express **17**, 7549–7555 (2009).
26. J. Tao, X. G. Huang, and J. H. Zhu, "A wavelength demultiplexing structure based on metal-dielectric-metal plasmonic nanocapillary resonators," Opt. Express **18**, 11111–11116 (2010).
27. F. Hu, H. Yi, and Z. Zhou, "Wavelength demultiplexing structure based on arrayed plasmonic slot cavities," Opt. Lett. **36**, 1500–1502 (2011).
28. J. Tao, X. G. Huang, X. Lin, Q. Zhang, and X. Jin, "A narrow-band subwavelength plasmonic waveguide filter with asymmetrical multiple-teeth-shaped structure," Opt. Express **17**, 13989–13994 (2009).
29. X. S. Lin and X. G. Huang, "Tooth-shaped plasmonic waveguide filters with nanometeric sizes," Opt. Lett. **33**, 2874–2876 (2008).
30. S. R. Mirnaziry, A. Setayesh, and M. S. Abrishamian, "Design and analysis of plasmonic filters based on stubs," J. Opt. Soc. Am. B **28**, 1300–1307 (2011).
31. E. Economou, "Surface plasmons in thin films," Phys. Rev. **182**, 539 (1969).
32. H. A. Haus, *Waves and Fields in Optoelectronics* (Prentice-Hall, 1984), Vol. **1**.